INORGANIC CHEMISTRY FRONTIERS

RESEARCH ARTICLE

View Article Online
View Journal

Cite this: DOI: 10.1039/d5qi00422e

Structural engineering of MXene frameworks with abundant surface functionalities for enhanced lithium–sulfur battery electrochemistry†

Yongjie Ye,[a] Sisi Liu,[a] Yongqian He,[a] Wanqi Zhang,[a] Ying Chen,[a] Mengqing Wang,[a] Xuewen Peng,[a] Caixiang Wang,[a] Qin Tang,[a] Yan Luo,[a] Bing Wu, *[b] Hongbo Shu,[a] Ruizhi Yu *[c] and Manfang Chen *[a]

Two-dimensional MXene materials have garnered significant attention in lithium–sulfur battery (LSBs) research due to their inherent high electrical conductivity and exceptional catalytic activity, which help mitigate the intrinsic challenges of sluggish redox kinetics and polysulfide shuttling. However, systematic investigations into the correlation between the structural evolution of MXene-based electrodes and their electrochemical performance remain underdeveloped. In this study, $Ti_3C_2T_x$ and Ti_2CT_x are fabricated *via* a top-down method, and their performance differences in LSBs are compared. Due to its unique three-layer titanium atomic structure and rich surface functional groups (–OH, –O, –F, *etc.*), $Ti_3C_2T_x$ exhibits excellent conductivity and chemical stability. Electrochemical testing and *in situ* ultraviolet–visible spectroscopy analysis show that $Ti_3C_2T_x$ effectively suppresses the polysulfide shuttle effect and accelerates the redox conversion of sulfur species. The cell using $Ti_3C_2T_x$ as a separator exhibits a capacity decay rate of 0.085% at 2 C after 200 cycles, and it maintains stable cycling at 60 °C, in contrast to Ti_2CT_x, which fails after 50 cycles. This study highlights how structural differences in MXene materials influence the electrochemical behavior of LSBs, providing new insights and establishing a foundation for their application in high-performance LSBs.

Received 11th February 2025,
Accepted 17th April 2025

DOI: 10.1039/d5qi00422e

rsc.li/frontiers-inorganic

1. Introduction

With the intensifying global energy crisis and worsening environmental pollution, there is a pressing demand for the development of next-generation, green, and durable energy storage materials.[1–4] Lithium–sulfur batteries (LSBs), offering an outstanding theoretical specific capacity of approximately 1675 mA h g^{-1} [5] and a significant theoretical energy density of about 2600 W h kg^{-1},[6] are regarded as promising candidates for next-generation high-energy-density energy storage systems.[7] However, unlike the simple intercalation electrochemistry of lithium-ion batteries,[8] LSBs operate through a completely reversible reaction between S_8 and metallic lithium.[9] Therefore, several challenges inevitably arise in practical applications, including: (1) the shuttle effect of polysulfides (LiPSs),[10] (2) the insulating nature and substantial volume fluctuations of lithium sulfide and sulfur,[11] and (3) the growth of dendritic lithium structures.[12]

To address the aforementioned issues, researchers typically focus on improving the cathode material construction,[13] modifying the separator coating layer,[14] and optimizing the electrolyte.[15] Among these approaches, modifying the separator coating layer does not require complex structural design, and the preparation process is relatively simple, making it favored by researchers. The development of multifunctional separator materials is expected to overcome the aforementioned issues and yield higher-performance LSBs.[16] In the early development of separator coating modification, two-dimensional graphite-based carbon materials[17] were recognized by researchers for their excellent conductivity and adsorption properties, and were applied to modify separator materials. However, since these materials are nonpolar, their interaction with the polar LiPSs is weak.[18,19] Therefore, polar materials such as TiO_2[20] and BN[21] have been applied to strengthen the interaction with LiPSs. In spite of this, the accumulation of a large amount of

[a]National Base for International Science & Technology Cooperation of New Energy Equipment, Energy Storage Materials and Devices; National Local Joint Engineering Laboratory for Key Materials of New Energy Storage Battery; Hunan Province Key Laboratory of Electrochemical Energy Storage & Conversion; School of Chemistry, Xiangtan University, Xiangtan 411105, Hunan, China. E-mail: mfchen@xtu.edu.cn
[b]Department of Inorganic Chemistry, University of Chemistry and Technology Prague, Technická 5, Prague 6, 166 28, Czech Republic. E-mail: wui@vscht.cz
[c]Institute of Micro/Nano Materials and Devices, Ningbo University of Technology, Ningbo, Zhejiang 315211, China. E-mail: ruizhi.yu@nbut.edu.cn

† Electronic supplementary information (ESI) available. See DOI: https://doi.org/10.1039/d5qi00422e

LiPSs in the cathode and separator materials still leads to the loss of active materials. In recent years, materials that catalytically convert LiPSs have gradually been discovered and widely applied in LSBs. Two-dimensional materials, owing to their large specific surface reactivity and tunable surface chemical properties, have been extensively applied in separator materials.[22]

MXenes are a category of two-dimensional materials incorporating transition metals (M) and carbon or nitrogen (X), characterized by a distinctive layered structure. Their chemical formula is typically identified as $M_{n+1}X_nT_x$, where M denotes transition metal elements (such as Ti, Nb, Zr, *etc.*), X indicates carbon or nitrogen, and T refers to surface functional groups (such as –OH, –O, –F, *etc.*).[23] MXenes have become a prominent research focus for LSB separator materials in recent years, owing to their exceptional electrical conductivity, layered architecture, and abundant surface functional groups.[24–26] MXene materials, particularly $Ti_3C_2T_x$ and Ti_2CT_x, are widely regarded as excellent battery materials thanks to their exceptional two-dimensional structure and highly adjustable surface chemical properties. Moreover, the surface of MXenes can be chemically modified to incorporate a diverse set of functional groups (such as –OH, –O, –F, –Cl, *etc.*).[27,28] The functional groups on the surface, along with the anchoring of metals and other active components, can adjust the conductivity and structural properties of MXenes. Wei *et al.*[29] found that completely bare MXene materials were not favorable for LiPS adsorption. In contrast, MXene materials with surface functional groups play an essential role in interacting with LiPSs, with the adsorption strength following the order: S > O > N > F > Cl. Zhang *et al.*[30] synthesized $TiOF/Ti_3C_2$ MXene nanoribbons *via* a fluorination method and, through computational science and electrochemical analysis, demonstrated that F activates the catalytic role of Ti in the continuous redox reactions of active sulfur, stemming from Lewis acid–base interactions. The experimental results showed that after 500 charge–discharge cycles, the $TiOF/Ti_3C_2$ battery exhibited an initial discharge capacity of 868.3 mA h g^{-1}, a maintained discharge capacity of 486.2 mA h g^{-1}, and a cycling decay rate of 0.088%.

$Ti_3C_2T_x$ and Ti_2CT_x, as two typical MXene materials, exhibit significant differences in the number and types of surface functional groups.[31–33] These differences directly influence their interactions with LiPSs, their Li^+ transport properties, and the cycling performance of the battery. Furthermore, the structural differences between $Ti_3C_2T_x$ and Ti_2CT_x, such as the number of titanium layers, also play a vital role in electrical conductivity and structural stability, which are essential factors for improving the efficiency and cycle life of LSBs. Despite the potential of MXenes in LSBs, systematic studies comparing the electrochemical performance of $Ti_3C_2T_x$ and Ti_2CT_x, especially in relation to their structural differences, remain scarce.

In this study, two MXene materials, $Ti_3C_2T_x$ and Ti_2CT_x, are synthesized through a top-down method. Thanks to its exceptional structure and plentiful surface functional groups, $Ti_3C_2T_x$ exhibits higher conductivity compared to Ti_2CT_x. Structural analysis reveals that $Ti_3C_2T_x$ contains abundant O and F functional groups, leading to a significant shift in the binding energy in the Ti 2p region scan spectrum. Benefiting from its higher conductivity and rich surface functional groups, $Ti_3C_2T_x$ demonstrates better sulfur redox kinetics. *In situ* UV-Vis testing indicates that $Ti_3C_2T_x$ contains more S_8^{2-} and $S_3^{\bullet-}$ radicals, thereby promoting the catalytic transformation of LiPSs. The battery with a $Ti_3C_2T_x$ separator exhibits excellent electrochemical efficiency. At a current density of 0.1 C, the cell with $Ti_3C_2T_x$ exhibits a discharge capacity of 1263.8 mA h g^{-1}, with a cycle degradation rate of just 0.066% after 50 cycles. Under high-temperature conditions of 60 °C, the cell with $Ti_3C_2T_x$ demonstrates superior cycling stability compared to the cell with Ti_2CT_x, which deactivates after 50 cycles. This groundbreaking study provides further insights into the structural differences of MXenes and their impact on performance, enhancing the understanding of their structural properties and contributing valuable knowledge for the design of high-performance LSBs.

2. Experimental

2.1 Material characterization

The surface morphology of the sample was thoroughly investigated using a field emission scanning electron microscope (FESEM S-4800, Hitachi, Japan). Transmission electron microscopy (TEM, FEI TF20, Netherlands) was used for further analysis of the sample lattice. X-ray diffraction (XRD) characterization was performed to determine the physical composition of the material. X-ray photoelectron spectroscopy (XPS, PHI 5000 Versa Probe, Japan) was employed to acquire the surface elemental composition and valence states of the samples. The sulfur content was determined using a thermogravimetric analyzer (TGA) under a N_2 atmosphere. The electronic resistivity of powder materials was measured using a four-probe tester (ST2742B, Lattice Electronics Suzhou, China).

2.2 Preparation of $Ti_3C_2T_x/Ti_2CT_x$

Ti_3AlC_2 was etched at room temperature with HF acid for one week, then washed thoroughly and placed in a 20% TBAOH solution for stirring and exfoliation for 3 days. Centrifugation was performed at below 1000 rpm to remove the material that had not been fully etched or exfoliated. The solids in the suspension were collected, freeze-dried, and then stored under an argon atmosphere, yielding $Ti_3C_2T_x$. The preparation method for Ti_2CT_x is similar to that for $Ti_3C_2T_x$, with the difference being the replacement of the MAX phase with Ti_2AlC.

2.3 Synthesis of an MXene separator

The MXene-coated separator was fabricated by mixing polyvinylidene fluoride (PVDF) and Super P (SP) with MXenes in a weight ratio of 1 : 2 : 7. The components were thoroughly dispersed in *N*-methylpyrrolidone (NMP) to form a uniform slurry. This slurry was then applied onto a Celgard polypropylene (PP) film *via* a coating process. After coating, the PP separator was positioned in a drying oven at 40 °C for 12 hours to ensure complete evaporation of the solvent and secure adhesion of the MXene coating.

2.4 Preparation of a cathode

To prepare the cathode material for the LSBs, carbon nanotubes (CNTs, sourced from Cnano Technology) and sublimed sulfur were mixed uniformly in a 4 : 1 weight ratio and heated at 155 °C for 12 hours to form the CNT/S composite. This CNT/S mixture was then blended with PVDF and SP with a weight ratio of 7 : 2 : 1 in an NMP solution to create a slurry. The slurry was subsequently evenly applied to carbon-coated aluminum foil, which was dried at 60 °C for 12 hours under vacuum conditions to remove residual solvent. After drying, the foil was sliced into disks, each with a diameter of 10 mm, resulting in a sulfur loading of 1.4 mg cm^{-2}. For cathodes with higher sulfur loading (5.68 mg cm^{-2}), the slurry was then applied to carbon paper (sourced from Toray) using the same procedure.

2.5 Electrochemical measurements

The cell battery consisted of a CNT/S cathode, modified separator material, electrolyte, and a lithium metal anode. The electrolyte was synthesized by combining 1 mol L^{-1} lithium bis(trifluoromethylsulfonyl)imide (LiTFSI) with 2% $LiNO_3$ in a solvent blend of 1,3-dioxolane (DOL) and dimethoxymethane (DME) at a 1 : 1 volume ratio. Cyclic voltammetry (CV) measurements were conducted within a voltage range of 1.7 to 2.8 V. Electrochemical impedance spectroscopy (EIS) was performed over a frequency range of 10^5 Hz to 10 mHz using a CHI 750 electrochemical workstation. Charge/discharge tests were performed across a voltage range from 1.7 to 2.8 V using the Neware battery test system.

2.6 Preparation of Li_2S_6 and a symmetric battery

A 0.1 mol L^{-1} Li_2S_6 solution was synthesized by dissolving sulfur and lithium sulfide in a 5 : 1 molar ratio in a DME/DOL (1 : 1 v/v) solvent. The MXene material and PVDF were ground and then dissolved in an NMP solution in a 9 : 1 weight ratio to obtain the slurry for the cathode material. The slurry was then evenly applied to carbon-coated aluminum foil to form the symmetric electrodes. The symmetric cell consisted of two cathodes with identical mass, a Celgard 2500 separator, and the Li_2S_6 electrolyte. The electrochemical performance of the symmetric cell was assessed using a CHI750 electrochemical workstation. Cyclic voltammetry was conducted at a scan rate of 10 mV s^{-1} within a voltage range of −1.0 to 1.0 V.

2.7 Preparation of Li_2S_8 and measurements of Li_2S precipitation (dissolution)

A 0.1 mol L^{-1} Li_2S_8 solution was synthesized by dissolving sulfur and lithium sulfide in a 7 : 1 molar ratio in a solvent mixture of DME/DOL (1 : 1 v/v). The preparation of the cathode material was similar to that of the symmetric cell, with the difference being that the cathode material was coated onto carbon paper. The deposition/dissolution experiment of Li_2S was conducted using a coin cell structure, which included a cathode loaded with the MXene material, a Celgard 2400 PP separator, a lithium metal anode, and the Li_2S_8 solution. During the preparation of the coin cell, 25 μL of the Li_2S_8 solution was added onto the cathode material, and 25 μL of the LiTFSI electrolyte was added onto the anode. The deposition (dissolution) test of Li_2S was performed by discharging at a constant current of 0.112 mA to 2.06 V (1.7 V), followed by constant potential charge and discharge at 2.05 V (2.4 V) for 80 000 seconds.

2.8 *In situ* ultraviolet–visible (*in situ* UV-Vis) spectral measurement

The preparation of sulfur-based cathode materials is similar to that of conventional coin cells, with the key difference being the substitution of CNTs with MXene materials. The materials were subsequently cut to dimensions of 0.8 cm × 1.5 cm and functioned as the cathode for the *in situ* UV-visible battery. The sulfur loading on the cathode was estimated to be around 4.5 mg cm^{-2}. Subsequently, inside an argon-filled glove box, the MXene material was employed as the cathode, lithium metal was employed as the anode, and the components were assembled with Li–S electrolyte into a custom-designed *in situ* cuvette to construct the *in situ* UV-visible battery. The electrochemical workstation was connected to the *in situ* cuvette, and constant current discharge at 0.05 C was applied. The UV-visible spectrometer recorded spectral data in the range of 400–700 nm every 15 minutes to monitor the battery performance in real time.

2.9 First-principles calculations

First-principles calculations were performed using the GPAW + ASE framework with the PBE functional. A 4 × 4 × 1 supercell of monolayer Ti_2CO_2 and $Ti_3C_2O_2$ was constructed, with a 20 Å vacuum layer added along the *z*-direction to prevent interlayer interactions.[34] Gamma-only *k*-point sampling was applied, and the plane-wave cutoff energy was set to 450 eV. Structural optimization was carried out using the BFGS optimizer, where the bottom three atomic layers of the slab were fixed, allowing the remaining atoms to fully relax. The convergence criteria for structure relaxation were set to an energy threshold of 5×10^{-5} eV per atom, an eigenstate convergence of 1.0×10^{-6} eV, and a force criterion of 0.05 eV $Å^{-1}$.[35]

The adsorption energy (E_{ads}) was calculated using the following equation:

$$E_{ads} = E_{total} - E_{lips} - E_{sur}$$

where E_{total} represents the total energy of the adsorption system, E_{lips} is the energy of the isolated adsorbate, and E_{sur} denotes the energy of the pristine substrate.

3. Results and discussion

As illustrated in Fig. 1a, the $Ti_3C_2T_x$ and Ti_2CT_x materials are synthesized using a top-down etching method, where MAX

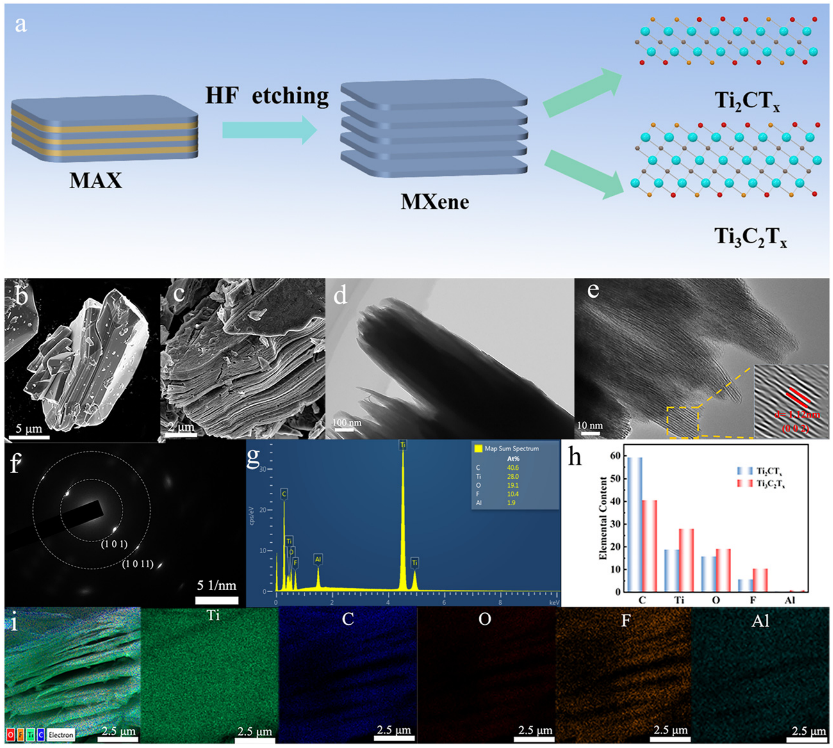

Fig. 1 (a) Procedure for the synthesis of MXenes. (b) SEM maps of Ti_3AlC_2 and (c) $Ti_3C_2T_x$. (d) TEM, (e) HRTEM, and (f) SAED diffractograms of $Ti_3C_2T_x$. (g) EDS mapping of $Ti_3C_2T_x$. (h) MXene surface functional group content. (i) EDS elemental mapping of $Ti_3C_2T_x$. (For SEM and TEM examinations, three distinct areas are chosen.)

phase materials (Ti_3AlC_2 and Ti_2AlC) are etched at room temperature using hydrofluoric acid solution.[36] To examine the microstructure of the materials, scanning electron microscopy (SEM) and transmission electron microscopy (TEM) are utilized for analysis. Fig. 1b and Fig. S1a† display the SEM images of Ti_3AlC_2 and Ti_2AlC, where the MAX phase materials exhibit a block-like structure. After etching, the MXene materials exhibit significant delamination, especially $Ti_3C_2T_x$, which shows a relatively smooth surface (as shown in Fig. 1c and Fig. S1b†). This difference may be attributed to the higher content of surface functional groups (such as O and F) on $Ti_3C_2T_x$. The increased surface functional groups not only enhance the chemical reactivity of the material but may also result in a more uniform and porous surface. Further TEM observations (Fig. 1d) reveal that $Ti_3C_2T_x$ exhibits a typical layered structure with distinct interlayer gaps. High-resolution TEM (HRTEM) images (Fig. 1e) further show that the lattice spacing of $Ti_3C_2T_x$ is 1.12 nm, corresponding to the (0 0 2) plane of $Ti_3C_2T_x$.[37] Selected area electron diffraction (SAED) reveals diffraction rings that correspond to the (1 0 1) and (1 0 11) planes of $Ti_3C_2T_x$, further confirming the existence of its layered structure. To obtain a more thorough understanding of the elemental composition of the MXene materials, energy dispersive X-ray spectroscopy (EDS) analysis is performed (Fig. 1g and Fig. S2a†). The analysis clearly shows the elemental composition of $Ti_3C_2T_x$ and Ti_2CT_x, where $Ti_3C_2T_x$ has a higher titanium content compared to Ti_2CT_x and contains a significant amount of surface functional groups like O and F (Fig. 1h). Furthermore, elemental mapping images (Fig. 1i and Fig. S2b, c†) indicate that Ti, C, O, F, and other elements are evenly distributed throughout the MXene materials, with a trace amount of unetched Al observed.

To further investigate the physical properties of $Ti_3C_2T_x$ and Ti_2CT_x, Fig. 2a presents the results of the resistivity of MXene materials as a function of pressure measured using a four-point probe method. As depicted in the bar chart comparison in Fig. 2b, the resistivity of $Ti_3C_2T_x$ is notably lower than that of Ti_2CT_x, exhibiting a difference of roughly tenfold. The lower resistivity suggests that $Ti_3C_2T_x$ possesses superior conductivity, which helps to enhance charge transfer rates and improve electron transport efficiency. The electronic structures of Ti_2CT_x and $Ti_3C_2T_x$ are further investigated by density of states (DOS) analysis. As shown in Fig. S3a and b,† the calculated bandgaps of Ti_2CT_x and $Ti_3C_2T_x$ are 0.512 eV and 0.466 eV, respectively. This observation may be attributed to the increased electron density in the d orbitals of Ti atoms, which enhances the metallic conductivity, as well as the rich surface functional groups in $Ti_3C_2T_x$. The narrower bandgap of $Ti_3C_2T_x$ suggests enhanced charge carrier mobility, which aligns with its superior electrical conductivity observed in the four-point probe measurements. Further X-ray diffraction (XRD) analysis (Fig. 2c) shows that the diffraction peaks of Ti_3AlC_2 and Ti_2AlC align with the MAX phase diffraction peaks in the PDF#00-052-0875 [38] and PDF#00-029-0095 [39] databases,

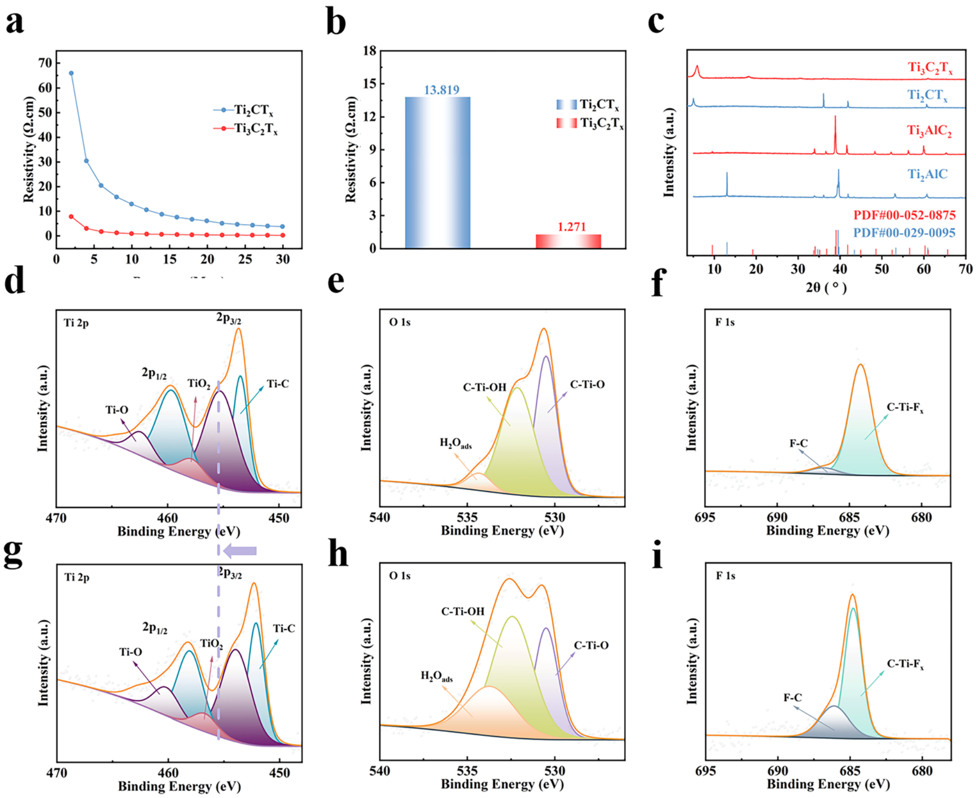

Fig. 2 (a) Resistivity and (b) mean resistivity of MXenes. (c) XRD patterns; XPS patterns of Ti_2CT_x: (d) Ti 2p, (e) O 1s and (f) F 1s; and XPS patterns of $Ti_3C_2T_x$: (g) Ti 2p, (h) O 1s, and (i) F 1s. (The dataset is derived from three independent experimental replicates.)

respectively. After acid etching, the MXene materials lose the characteristic diffraction peaks of the MAX phase, indicating that the Al layer is gradually eliminated during the etching process, leading to the collapse of the MXene interlayer structure. Meanwhile, the (002) diffraction peak of the MAX phase exhibits a noticeable shift to the left, indicating an expansion of the interlayer spacing in MXenes compared to the MAX phase.[40] Additionally, it has been demonstrated through Fourier transform infrared spectroscopy (FTIR) that more functional groups are present in $Ti_3C_2T_x$ compared to Ti_2CT_x. As observed in Fig. S4,† the FTIR spectrum of $Ti_3C_2T_x$ exhibits distinct C–O stretching vibrations (~1630 cm^{-1}) and C–H vibrations (~1400 cm^{-1}). The intensity of the C–O peak is higher in the $Ti_3C_2T_x$ infrared spectrum, which suggests a higher oxygen content in $Ti_3C_2T_x$ to some extent.[33,41] The vibration peaks in the ranges of 450–350 cm^{-1} and 600–450 cm^{-1} correspond to the Ti–C and Ti–O bonds, respectively.[42]

As observed in Fig. S5a,† the X-ray photoelectron spectroscopy (XPS) full spectra analysis corroborates the existence of O and F functional groups on the MXene material surfaces. Quantitative analysis of the relative elemental composition obtained from XPS revealed distinct compositional differences between the materials. As summarized in Table S1,† the O/Ti ratio in $Ti_3C_2T_x$ demonstrates a significantly higher value of 1.32 compared to 0.87 for Ti_2CT_x, with similar enhancement trends observed in F/Ti ratios based on XPS measurements. The XPS-derived surface compositional features are further corroborated by the above FTIR spectroscopy results, which confirm the presence of abundant surface functional groups in the $Ti_3C_2T_x$ structure. A further comparison of the Ti 2p region scan spectra of $Ti_3C_2T_x$ and Ti_2CT_x (Fig. 2d and g) reveals a significant shift in the Ti 2p binding energy to higher values for Ti_2CT_x compared to $Ti_3C_2T_x$. This change is attributed to the fact that Ti_2CT_x is more prone to oxidation in air compared to $Ti_3C_2T_x$, causing its Ti 2p peak to shift to a higher binding energy.[33,43] Additionally, we fitted a TiO_2 peak at approximately 458.2 eV, and the peak area for Ti_2CT_x was larger, further confirming the issue of Ti_2CT_x being more prone to oxidation in air.[44] Fig. S5b and c† show the C 1s region scan spectra for Ti_2CT_x and $Ti_3C_2T_x$, where the different peaks can be assigned to C–Ti, Ti–O, C–C, C–O, and O–C=O bonds.[45] In the analysis of O elements, Fig. 2e and f display the O 1s region scan spectrum. Near 532.4 eV, the peak intensity of $Ti_3C_2T_x$ is significantly higher than that of Ti_2CT_x, with this difference being ascribed to the higher concentration of O functional groups in $Ti_3C_2T_x$, especially the presence of C–Ti–OH bonds. Additionally, $Ti_3C_2T_x$ and Ti_2CT_x exhibit two peaks at 530.5 eV and 533.7 eV, corresponding to C–Ti–O and surface adsorbed oxygen (Oads). This is likely due to moisture adsorption by the material from the air.[46] Furthermore, the F 1s region scan spectra in Fig. 2f–i indicate that the F 1s peaks of

Ti_2CT_x and $Ti_3C_2T_x$ at 684.7 eV and 686.1 eV correspond to C–Ti–F_x and F–C bonds, further validating the abundance of F functional groups on the surface of $Ti_3C_2T_x$.[47]

LiPSs typically undergo multiple processes, such as adsorption and conversion, with each step being crucial to the overall performance of the battery. To further examine the ability of MXene materials to adsorb LiPSs, a visual adsorption experiment of Li_2S_6 is first conducted, followed by ultraviolet–visible absorption spectroscopy of the post-adsorption solution. As shown in Fig. 3a, the inset illustrates that after 1 hour of adsorption, the solution of $Ti_3C_2T_x$ + Li_2S_6 is clearer compared to Ti_2CT_x + Li_2S_6, and the ultraviolet–visible spectrum reveals a lower absorption peak intensity for $Ti_3C_2T_x$ + Li_2S_6, indicating that $Ti_3C_2T_x$ exhibits stronger adsorption capability for Li_2S_6. This result suggests that $Ti_3C_2T_x$ effectively suppresses the LiPSs shuttle effect. Further validation of the electrochemical conversion capability of $Ti_3C_2T_x$ is conducted through cyclic voltammetry (CV) tests on symmetric cells. As can be seen in Fig. 3b, $Ti_3C_2T_x$ exhibits higher peak currents and a larger integrated current area in the CV curve, indicating its excellent catalytic ability in the conversion of LiPSs. This characteristic is closely related to the stronger electrochemical activity and better electronic conductivity of $Ti_3C_2T_x$. To further investigate the interaction between MXenes and LiPSs, the adsorption energy of Li_2S_8 is calculated through differential charge density analysis from both side views (Fig. 3c and d) and top views (Fig. S6a and b†). O-terminated surfaces, including $Ti_3C_2O_2$ and Ti_2CO_2, were selected as the most stable terminal groups.[48] The calculation of adsorption energies show that $Ti_3C_2O_2$ has an adsorption energy of −1.16 eV, while Ti_2CO_2 has an adsorption energy of −0.85 eV, indicating that $Ti_3C_2T_x$, which contains more surface functional groups, has a stronger Li_2S_8 adsorption ability. To further evaluate the catalytic activity of $Ti_3C_2T_x$, Li_2S deposition and dissolution experiments are performed. In Fig. 3e and f, $Ti_3C_2T_x$ shows a higher Li_2S nucleation capacity of 284.8 mA h g^{-1}, significantly outperforming Ti_2CT_x (263.5 mA h g^{-1}). Additionally, the Li_2S nucleation time for $Ti_3C_2T_x$ is 203 seconds, noticeably shorter than that of Ti_2CT_x (Fig. 3f). This result suggests that $Ti_3C_2T_x$ has faster electrochemical reaction kinetics, enabling it to more efficiently facilitate the nucleation of Li_2S. In the Li_2S dissolution experiment (Fig. 3g and h), $Ti_3C_2T_x$ demonstrates

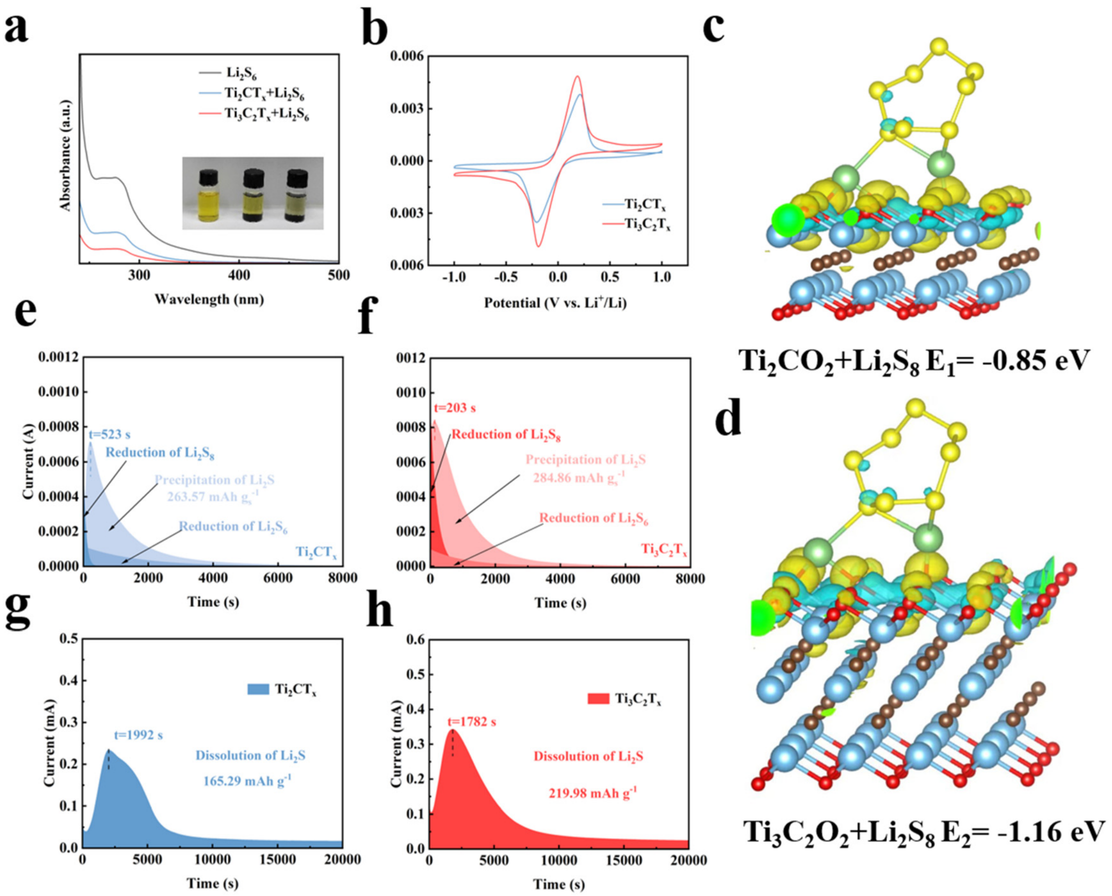

Fig. 3 (a) UV-Vis spectrum (illustration: visualized experiment). (b) Symmetric cell. Side view of the differential charge density for the adsorption of Li_2S_8 on (c) Ti_2CO_2 and (d) $Ti_3C_2O_2$ (yellow represents electron accumulation; indigo blue represents the electron depletion region). Li_2S deposition curves of (e) $Ti_3C_2T_x$ and (f) Ti_2CT_x; Li_2S dissolution curves of (g) $Ti_3C_2T_x$ and (h) Ti_2CT_x. (The presented dataset is generated through a series of more than five independent experimental replicates.)

superior dissolution capabilities compared to Ti_2CT_x. Specifically, the dissolution time of $Ti_3C_2T_x$ is 1782 seconds, with a dissolution capacity of 219.9 mA h g^{-1}, both of which outperform Ti_2CT_x, which shows 1992 seconds and 165.2 mA h g^{-1}, respectively. This further confirms that $Ti_3C_2T_x$ demonstrates enhanced catalytic activity in the transformation of LiPSs. This experimental result is consistent with the calculated adsorption energy of Li_2S_8 mentioned above. As depicted in Fig. S7,† the sulfur content in the CNT/S cathode material is 82 wt%. In this system, MXene materials, as modified separators in LSBs, can effectively facilitate the transformation of Li_2S. To further verify the effect of $Ti_3C_2T_x$ on the redox conversion of Li_2S, the galvanostatic intermittent titration technique (GITT) is performed (Fig. S8a and b†). Compared to the battery with the Ti_2CT_x separator material (45.6 and 53.8 mV potential difference), the $Ti_3C_2T_x$ battery displays a lower potential difference (41.3 and 43.4 mV) under the same test conditions, indicating that $Ti_3C_2T_x$ can significantly reduce the nucleation overpotential of Li_2S. Through GITT analysis (Fig. S8c†), the internal resistance for the nucleation of Li_2S is further calculated. The results show that $Ti_3C_2T_x$ has significantly lower internal resistance for Li_2S nucleation compared to Ti_2CT_x, indicating its ability to effectively reduce the nucleation overpotential of Li_2S.

Fig. S9a and b† show the electrochemical impedance spectra (EIS) of MXene materials before and after cycling. It can be observed from the figure that a new semicircle appears in the EIS spectrum after cycling, with the first semicircle corresponding to the charge transfer resistance (R_{ct}) and the second semicircle representing the polarization resistance (R_p).[49] Since LSBs involve a 16-electron reversible electrochemical reaction, the information in the EIS spectrum is limited for in-depth analysis of the electrochemical behavior of the battery. Therefore, to gain a deeper understanding, distribution of relaxation time (DRT) analysis is introduced to further interpret the EIS data.[50] As observed in Fig. 4a and b, DRT analysis before and after cycling indicates that the Li^+ diffusion resistance of $Ti_3C_2T_x$ is significantly lower than that of Ti_2CT_x. Before cycling, the Li^+ diffusion resistance of $Ti_3C_2T_x$ is 1382.3 Ω, whereas for Ti_2CT_x, it is 1504.8 Ω. After 30 cycles, the LiPS diffusion resistance of $Ti_3C_2T_x$ is 2.3 Ω, significantly lower than the 5.4 Ω of Ti_2CT_x. This is because the inherent metallic conductivity of $Ti_3C_2T_x$ significantly accelerates charge transfer kinetics. Meanwhile, the abundant surface functional groups of $Ti_3C_2T_x$ interact with LiPSs during cycling, leading to the detachment of some functional groups. This process exposes the highly conductive MXenes, while the C–Ti–O functional groups act as electron transfer bridges, synergistically enhancing the overall conductivity, thereby resulting in a significant reduction in its diffusion impedance. To gain a more comprehensive understanding of the electrochemical behavior of MXene materials at various temperatures, EIS tests are conducted at various temperatures (Fig. 4c and Fig. S10†). Throughout the temperature span of 30 °C to 60 °C, the charge transfer resistance of $Ti_3C_2T_x$ remains lower than

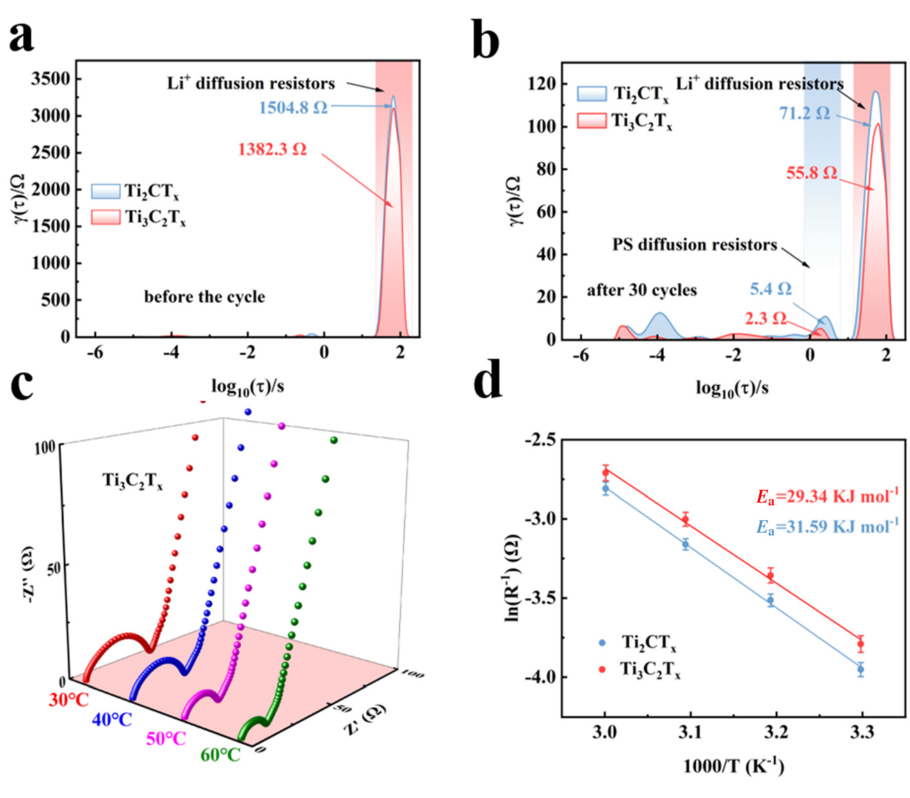

Fig. 4 DRT (a) before the cycle and (b) after 30 cycles. (c) EIS of $Ti_3C_2T_x$ at different temperatures. (d) Activation energy. (The presented dataset is generated through a series of more than five independent experimental replicates.)

that of Ti_2CT_x, indicating that $Ti_3C_2T_x$ exhibits better electrochemical activity over a broader temperature range. Furthermore, based on the EIS data at varying temperatures, the surface activation energy of both materials is calculated using the Arrhenius equation.[51] Fig. 4d clarifies the linear relationship between the reciprocal of absolute temperature and the inverse of charge transfer resistance. According to the results from this plot, the activation energy of $Ti_3C_2T_x$ (E_a = 29.34 kJ mol^{-1}) is significantly lower than that of Ti_2CT_x (E_a = 31.59 kJ mol^{-1}). This result indicates that $Ti_3C_2T_x$ can accelerate the kinetics of redox reactions, thereby exhibiting improved electrochemical reaction efficiency and reaction rate.

To further investigate the redox performance of MXene materials, CV tests are conducted, and their redox conversion capability for LiPSs is evaluated by analyzing the CV curves and contour plots (Fig. S11a and b†). As shown in Fig. 5a and b, $Ti_3C_2T_x$ exhibits higher peak current responses, and its contour plot brightness is markedly higher than that of Ti_2CT_x, indicating that $Ti_3C_2T_x$ has superior redox kinetic properties. The Li^+ diffusion coefficient is obtained through further analysis using the Randles–Sevcik equation.[52]

$$I_p = 2.69 \times 10^5 n^{3/2} A D_{Li^+}{}^{1/2} C_{Li^+} \nu^{1/2} \quad (1)$$

In the above equation, I_p represents the peak current in the CV curve, n is the number of electrons involved, A is the cathode area, D_{Li^+} is the Li^+ diffusion coefficient, C_{Li^+} is the concentration of Li^+, and ν is the scan rate. Fig. 5c shows the linear dependence of the peak current on the square root of the scan rate. The Li^+ diffusion coefficient, shown in the bar chart in Fig. 5d, is calculated by fitting this linear relationship. The results indicate that the Li^+ diffusion coefficient of $Ti_3C_2T_x$ is higher than that of Ti_2CT_x, further confirming that $Ti_3C_2T_x$ can more effectively promote the diffusion of Li^+. This may be attributed to $Ti_3C_2T_x$ having three Ti layers (whereas Ti_2CT_x has only two). In contrast, the more compact structure of Ti_2CT_x limits Li^+ diffusion and exacerbates polysulfide shuttle. Additionally, Fig. 5e shows a CV comparison of different materials at 0.1 mV s^{-1}, and the ΔE_L and ΔE_H bar charts in Fig. 5f further compare the polarization voltages of $Ti_3C_2T_x$ and Ti_2CT_x. The findings demonstrate that the polarization voltage of $Ti_3C_2T_x$ (0.327 V and 0.022 V) is significantly lower than that of Ti_2CT_x (0.402 V and 0.112 V), indicating that $Ti_3C_2T_x$ exhibits lower voltage loss in electrochemical reactions, thereby improving the durability and efficiency of the battery over cycles. Further Tafel slope analysis (Fig. 5g and i) also shows that $Ti_3C_2T_x$ exhibits lower Tafel slopes at peaks A, B, and C compared to Ti_2CT_x, confirming that $Ti_3C_2T_x$ has faster reaction kinetics and stronger catalytic activity in the conversion of LiPSs.

The performance of MXenes in electrochemical applications within LSB separators is evaluated through a series of

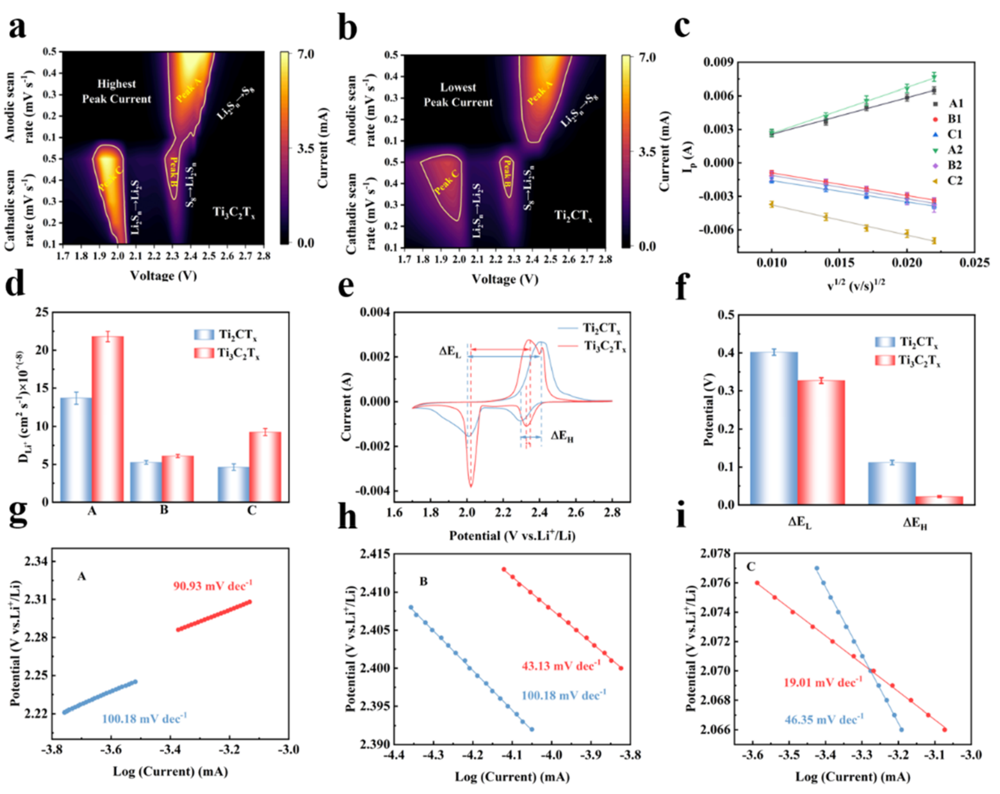

Fig. 5 CV contour plots of (a) $Ti_3C_2T_x$ and (b) Ti_2CT_x. (c) linear dependence between I_p and $\nu^{1/2}$. (d) Diffusion coefficient of Li^+. (e) CV comparison at 0.1 mV s^{-1}. (f) Bar chart of ΔE_H and ΔE_L. (g–i) Tafel slopes. (The presented dataset is generated through a series of more than five independent experimental replicates.)

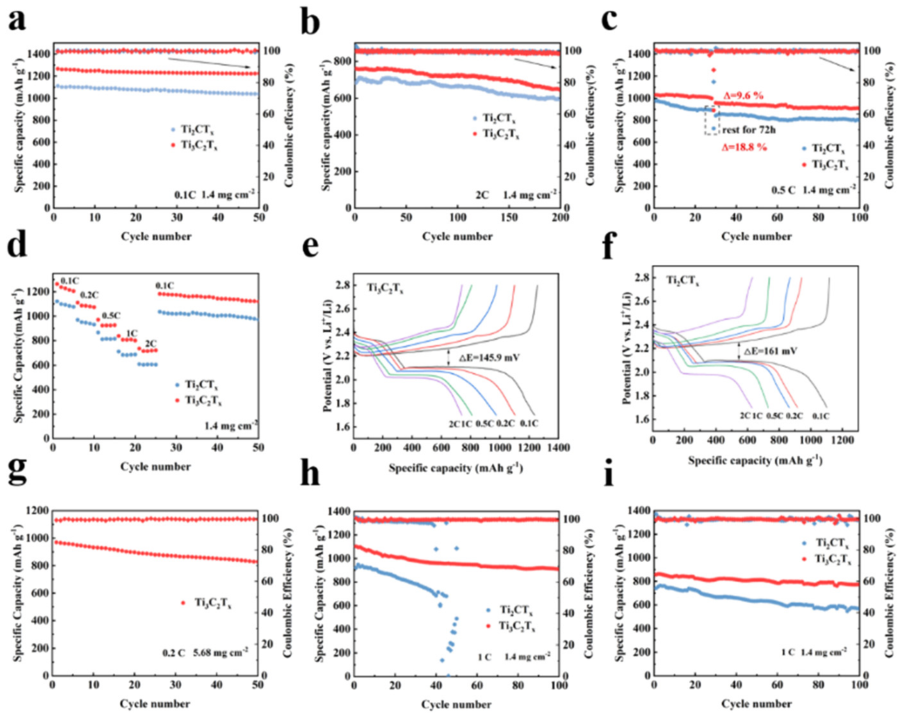

Fig. 6 Cycling performance of MXenes at (a) 0.1 C and (b) 2 C. (c) Self-discharge test at 0.5 C. (d) Rate performance. GCD curves at different rates of (e) $Ti_3C_2T_x$ and (f) Ti_2CT_x. (g) High sulfur loading. Cycling performance at (h) 60 °C and (i) 0 °C. (The presented dataset is generated through a series of more than five independent experimental replicates.)

cycling and rate performance tests. As observed in Fig. 6a, $Ti_3C_2T_x$ demonstrates an initial discharge capacity of 1263.8 mA h g^{-1} at 0.1 C, surpassing that of Ti_2CT_x (1110.6 mA h g^{-1}). Fig. 6b shows long-cycle performance at 2 C, where $Ti_3C_2T_x$ demonstrates higher cycling stability compared to Ti_2CT_x. This is likely ascribed to the abundant surface functional groups, including O and F, which enhance interface interactions with the electrolyte and electrode, thereby improving the overall stability of the battery. The self-discharge test of the battery at 0.5 C is depicted in Fig. 6c. After 30 cycles and resting for 72 hours, $Ti_3C_2T_x$ exhibits a decay rate of 9.6%, which is lower than that of Ti_2CT_x (18.8%). This indicates that $Ti_3C_2T_x$ can suppress LiPSs, effectively mitigating the self-discharge phenomenon of the battery. Rate performance testing is a crucial indicator for assessing the high-rate discharge capability of a battery. As shown in Fig. 6d, $Ti_3C_2T_x$ exhibits higher discharge capacity at different rates. At 0.1 C, $Ti_3C_2T_x$ has a discharge capacity of 1263.8 mA h g^{-1}, significantly higher than that of Ti_2CT_x (1121.6 mA h g^{-1}). Even under higher rates, $Ti_3C_2T_x$ maintains a better discharge capacity, with a value of 734.8 mA h g^{-1} at 2 C, while Ti_2CT_x shows only 609.6 mA h g^{-1}. Additionally, after the 2 C test, $Ti_3C_2T_x$ shows good recovery in discharge capacity (1182.5 mA h g^{-1}) when returned to 0.1 C, while Ti_2CT_x shows a significant decrease to 1035.4 mA h g^{-1}. This provides additional evidence that $Ti_3C_2T_x$ exhibits superior performance and higher reversibility at high rates. As summarized in Table S2,† the battery employing the $Ti_3C_2T_x$ separator demonstrates significant improvements in sulfur utilization, rate capability, and cycling stability compared to those employing commercial carbon-based and TiO_2-modified separators.[53–58] These enhanced electrochemical performances can be attributed to the superior electrical conductivity, abundant surface functional groups (–O, –OH, and –F terminations), and effective polysulfide anchoring capability of the $Ti_3C_2T_x$ material, where the surface moieties enable strong chemisorption of lithium LiPSs through Lewis acid–base interactions. Fig. 6e and f show the galvanostatic charge–discharge (GCD) curves of $Ti_3C_2T_x$ and Ti_2CT_x at different rates. At 0.1 C, the voltage polarization of $Ti_3C_2T_x$ (145.9 mV) is markedly lower than that of Ti_2CT_x (161.1 mV), confirming that $Ti_3C_2T_x$ exhibits a lower polarization voltage and a higher electrochemical reaction rate. By analyzing the GCD curves in Fig. S12a† and the ratio of the liquid–solid conversion platform (Q2) to the solid–liquid conversion platform (Q1) in Fig. S12b,† it can be observed that the Q2/Q1 ratio for $Ti_3C_2T_x$ is close to 3, indicating that it can more effectively promote redox reactions. As shown in Fig. S12c and d,† further analysis shows that the initial potential of $Ti_3C_2T_x$ (25 mV) is notably lower than that of Ti_2CT_x (50 mV), revealing that $Ti_3C_2T_x$ can initiate electrochemical reactions more rapidly and accelerate the conversion process at the liquid–solid interface. Additionally, its liquid–solid conversion overpotential is also lower (10.7 mV *vs.* 13.5 mV), further confirming its excellent electrochemical characteristics. Fig. 6g shows the cycling performance of $Ti_3C_2T_x$ at a 0.2 C rate with a sulfur loading of 5.68 mg cm^{-2}. After 50 cycles, $Ti_3C_2T_x$ still maintains a discharge capacity of 825.5 mA h g^{-1}, demonstrating good cycling stability. At a sulfur content of 5.75 mg cm^{-2}, the cell with the $Ti_3C_2T_x$ separator delivers specific discharge capacities of 1014.5, 799.8, and 619.1 mA h g^{-1} at current densities of 0.2 C, 0.5 C, and 1 C, respectively (Fig. S13a†). Notably, when the current density is restored to 0.2 C, the capacity recovers to 957.1 mA h g^{-1}, indicating superior rate capability even under high sulfur loading conditions. Apparently, the cell with the $Ti_3C_2T_x$ separator displays two distinct discharge plateaus even at 1 C, suggesting a fast redox conversion (Fig. S13b†). The high sulfur content 3D radar chart of this material compared with other $Ti_3C_2T_x$ MXene materials in Fig. S14† further highlights its practical advantages in the commercialization process.[30,59–65] To further investigate the material performance in practical applications, cycling tests are conducted under both high- and low-temperature conditions. As shown in Fig. 6h and i, under high-temperature conditions of 60 °C, Ti_2CT_x exhibits battery deactivation after 50 cycles, while $Ti_3C_2T_x$ can stably cycle for 100 cycles, indicating its superior stability at high temperatures. This advantage can be attributed to the three-layer Ti atomic structure of $Ti_3C_2T_x$, which provides abundant catalytic active sites and enhances the cycling stability of the battery through strong interactions between surface functional groups and the electrolyte. On the other hand, at low temperatures of 0 °C, after 100 cycles, $Ti_3C_2T_x$ exhibits a lower cycling decay rate (0.097% *vs.* 0.235%), further demonstrating its superior cycling stability under low-temperature conditions. Additionally, the performance of other MXene/S cathode materials was compared with that of the cell using the $Ti_3C_2T_x$ separator (as shown in Table S3†), further demonstrating the superior applicability of the cell using the $Ti_3C_2T_x$ separator with abundant surface functional groups in the field of energy storage.[66–71]

In situ UV-Vis spectroscopy can reveal the dynamic concentration changes of LiPSs during the charge–discharge process, further elucidating their impact on battery performance and validating the catalytic conversion capability of MXene materials towards LiPSs. Previous studies generally suggest that solid S_8 first converts into long-chain LiPSs, which then transform into short-chain LiPSs. During this conversion process, the $S_3^{\bullet -}$ radical not only helps to open the cyclic S_8 but also plays a crucial role in the transformation of long-chain LiPSs into short-chain LiPSs. The related conversion processes can be expressed by the following equations.[72–74]

$$(1)\ S_8 + 2e^- \rightarrow {S_8}^{2-} \qquad (2)$$

$$(2)\ {S_8}^{2-} \rightarrow {S_6}^{2-} + 1/4S_8 \qquad (3)$$

$$(3)\ {S_6}^{2-} \rightarrow 2{S_3}^{\bullet -} \qquad (4)$$

$$(4)\ {S_3}^{\bullet -} + 2e^- \rightarrow {S_3}^{2-} \qquad (5)$$

$$(5)\ 2{S_3}^{\bullet -} + 2{S_3}^{2-} \rightarrow {S_4}^{2-} \qquad (6)$$

As shown in Fig. 7a and c, the *in situ* UV-Vis spectra illustrate the alterations in the concentration of various sulfur species during the discharge process. Compared to Ti_2CT_x, $Ti_3C_2T_x$ shows significantly higher concentrations of ${S_8}^{2-}$ and ${S_3}^{\bullet -}$ during the discharge process, confirming that $Ti_3C_2T_x$ facilitates the catalytic transformation of LiPSs more effectively. Further analysis of the discharge curves (Fig. 7b and d) shows that $Ti_3C_2T_x$ exhibits a longer discharge time under a current density of 0.05 C, verifying that $Ti_3C_2T_x$ enhances the efficiency of sulfur species utilization, thereby optimizing the overall performance of the battery.

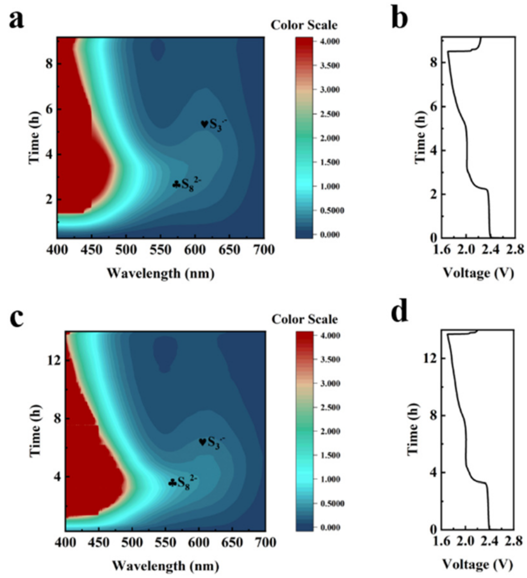

Fig. 7 *In situ* UV-Vis testing of (a) Ti_2CT_x, (c) $Ti_3C_2T_x$ and the corresponding discharge curves of (b) Ti_2CT_x and (d) $Ti_3C_2T_x$. (The presented dataset is generated through a series of more than five independent experimental replicates.)

4. Conclusion

In this study, $Ti_3C_2T_x$ and Ti_2CT_x are synthesized using a top-down approach, and their structural differences are systematically analyzed in terms of their impact on the electrochemical performance in LSBs. $Ti_3C_2T_x$, with its three-layer titanium atomic structure and abundant surface functional groups (O and F), demonstrates superior conductivity and chemical stability compared to Ti_2CT_x. Electrochemical analyses reveal that $Ti_3C_2T_x$ plays a critical role in mitigating the polysulfide shuttle effect, reducing the nucleation barrier of Li_2S, and facilitating the redox conversion of sulfur species. DRT tests before and after cycling show that $Ti_3C_2T_x$ has lower Li^+ and LiPS diffusion resistance. *In situ* UV-Vis testing results show that $Ti_3C_2T_x$ presents a greater concentration of ${S_3}^{\bullet -}$ radicals during the sulfur conversion process, indicating its ability to facilitate the conversion of LiPSs. Batteries using $Ti_3C_2T_x$ as a separator demonstrate a capacity decay rate of 0.066% after 50 cycles at a current density of 0.1 C and exhibit stable cycling performance under high-temperature conditions (60 °C). More importantly, even with a high sulfur content of 5.68 mg cm^{-2} and after 50 cycles, the capacity remains at 825.5 mA h g^{-1}.

This study offers valuable insights into the structural influences of MXenes on electrochemical performance, providing a deeper understanding that could accelerate the adoption of LSBs in high-performance applications.

Author contributions

Yongjie Ye: methodology, data curation, and writing – original draft. Sisi Liu: software. Yongqian He: investigation. Wanqi Zhang: investigation. Ying Chen: validation. Mengqing Wang: validation. Xuewen Peng: visualization. Caixiang Wang: visualization. Qin Tang: visualization. Yan Luo: validation. Bing Wu: supervision. Hongbo Shu: supervision. Ruizhi Yu: supervision. Manfang Chen: writing – review & editing.

Data availability

The original data supporting this article are available in the main text and the ESI.†

Conflicts of interest

The authors declare that they have no financial conflicts of interest or personal relationships that could have been perceived to influence the research presented in this paper.

Acknowledgements

We gratefully acknowledge the financial support from the National Natural Science Foundation of China (Grant No. 52172242 and 22309094), the Scientific Research Fund of the Hunan Provincial Department of Education (Grant No. 23B0126), and the Science & Technology Talents Lifting Project of Hunan Province (Grant No. 2023TJ-Z32); the Zhejiang Provincial Natural Science Foundation of China (No. LQ24B030010); the Ningbo Natural Science Foundation (No. 2023J388) and the Ningbo Yongjiang Talent Programme (No. 2023A-170-G); the ERC-CZ program (project LL2101) from the Ministry of Education Youth and Sports (MEYS); and the project Advanced Functional Nanorobots (Reg. No. CZ.02.1.01/0.0/0.0/15_003/0000444 financed by the EFRR). We also gratefully acknowledge Czech computer infrastructure Metacentrum provided by the e-INFRA CZ project (ID: 90254), supported by the Ministry of Education, Youth and Sports of the Czech Republic.

References

1 A. Manthiram, Y. Fu, S.-H. Chung, C. Zu and Y.-S. Su, Rechargeable Lithium–Sulfur Batteries, *Chem. Rev.*, 2014, **114**, 11751–11787.

2 T. Li, X. Bai, U. Gulzar, Y.-J. Bai, C. Capiglia, W. Deng, X. Zhou, Z. Liu, Z. Feng and R. Proietti Zaccaria, A Comprehensive Understanding of Lithium–Sulfur Battery Technology, *Adv. Funct. Mater.*, 2019, **29**, 1901730.

3 W. Zhang, J. Yin, W. Wang, Z. Bayhan and H. N. Alshareef, Status of rechargeable potassium batteries, *Nano Energy*, 2021, **83**, 105792.

4 J. Amici, P. Asinari, E. Ayerbe, P. Barboux, P. Bayle-Guillemaud, R. J. Behm, M. Berecibar, E. Berg, A. Bhowmik, S. Bodoardo, I. E. Castelli, I. Cekic-Laskovic, R. Christensen, S. Clark, R. Diehm, R. Dominko, M. Fichtner, A. A. Franco, A. Grimaud, N. Guillet, M. Hahlin, S. Hartmann, V. Heiries, K. Hermansson, A. Heuer, S. Jana, L. Jabbour, J. Kallo, A. Latz, H. Lorrmann, O. M. Løvvik, S. Lyonnard, M. Meeus, E. Paillard, S. Perraud, T. Placke, C. Punckt, O. Raccurt, J. Ruhland, E. Sheridan, H. Stein, J.-M. Tarascon, V. Trapp, T. Vegge, M. Weil, W. Wenzel, M. Winter, A. Wolf and K. Edström, A Roadmap for Transforming Research to Invent the Batteries of the Future Designed within the European Large Scale Research Initiative BATTERY 2030+, *Adv. Energy Mater.*, 2022, **12**, 2102785.

5 A. Hu, M. Zhou, T. Lei, Y. Hu, X. Du, C. Gong, C. Shu, J. Long, J. Zhu, W. Chen, X. Wang and J. Xiong, Optimizing Redox Reactions in Aprotic Lithium–Sulfur Batteries, *Adv. Energy Mater.*, 2020, **10**, 2002180.

6 J. Jiang, Q. Fan, S. Chou, Z. Guo, K. Konstantinov, H. Liu and J. Wang, Li2S-Based Li-Ion Sulfur Batteries: Progress and Prospects, *Small*, 2021, **17**, 1903934.

7 Y. Chen, T. Wang, H. Tian, D. Su, Q. Zhang and G. Wang, Advances in Lithium–Sulfur Batteries: From Academic Research to Commercial Viability, *Adv. Mater.*, 2021, **33**, 2003666.

8 X. Wu, Y. Liu, J. Wang, Y. Tan, Z. Liang and G. Zhou, Toward Circular Energy: Exploring Direct Regeneration for Lithium-Ion Battery Sustainability, *Adv. Mater.*, 2024, **36**, 2403818.

9 Z. W. Seh, Y. Sun, Q. Zhang and Y. Cui, Designing high-energy lithium–sulfur batteries, *Chem. Soc. Rev.*, 2016, **45**, 5605–5634.

10 R. Fang, S. Zhao, Z. Sun, D.-W. Wang, H.-M. Cheng and F. Li, More Reliable Lithium-Sulfur Batteries: Status, Solutions and Prospects, *Adv. Mater.*, 2017, **29**, 1606823.

11 W. Hua, H. Li, C. Pei, J. Xia, Y. Sun, C. Zhang, W. Lv, Y. Tao, Y. Jiao, B. Zhang, S.-Z. Qiao, Y. Wan and Q.-H. Yang, Selective Catalysis Remedies Polysulfide Shuttling in Lithium-Sulfur Batteries, *Adv. Mater.*, 2021, **33**, 2101006.

12 Y. He, D. Xiong, Y. Luo, W. Zhang, S. Liu, Y. Ye, M. Wang, Y. Chen, H. Liu, J. Wang, H. Lin, J. Su, X. Wang, H. Shu and M. Chen, Phase Reconstruction-Assisted Electron-Li+ Reservoirs Enable High-Performance Li-S Battery Operation Across Wide Temperature Range, *Adv. Funct. Mater.*, 2025, **35**, 2410899.

13 T. Zhang, L. Zhang, L. Zhao, X. Huang and Y. Hou, Catalytic Effects in the Cathode of Li-S Batteries: Accelerating polysulfides redox conversion, *EnergyChem*, 2020, **2**, 100036.

14 M. Xu, Q. Zhu, Y. Li, Y. Gao, N. Sun and B. Xu, Atom-dominated relay catalysis of high-entropy MXene promotes cascade polysulfide conversion for lithium–sulfur batteries, *Energy Environ. Sci.*, 2024, **17**, 7735–7748.
15 J. Guo, Q. Yang, Y. Dou, X. Ba, W. Wei and J. Liu, Shelf life of lithium–sulfur batteries under lean electrolytes: status and challenges, *Energy Environ. Sci.*, 2024, **17**, 1695–1724.
16 T. Zhao, P. Xiao, S. Nie, M. Luo, M. Zou and Y. Chen, Recent progress of metal-organic frameworks based high performance batteries separators: A review, *Coord. Chem. Rev.*, 2024, **502**, 215592.
17 L. Borchardt, M. Oschatz and S. Kaskel, Carbon Materials for Lithium Sulfur Batteries—Ten Critical Questions, *Chem. – Eur. J.*, 2016, **22**, 7324–7351.
18 G. Zhou, L.-C. Yin, D.-W. Wang, L. Li, S. Pei, I. R. Gentle, F. Li and H.-M. Cheng, Fibrous Hybrid of Graphene and Sulfur Nanocrystals for High-Performance Lithium–Sulfur Batteries, *ACS Nano*, 2013, **7**, 5367–5375.
19 M.-Q. Zhao, X.-F. Liu, Q. Zhang, G.-L. Tian, J.-Q. Huang, W. Zhu and F. Wei, Graphene/Single-Walled Carbon Nanotube Hybrids: One-Step Catalytic Growth and Applications for High-Rate Li–S Batteries, *ACS Nano*, 2012, **6**, 10759–10769.
20 S. Li, J. Liu, L. Ma, L.-J. Yu, L. Hou, D. Li, S. Gao, G. Yue, Z. Cui, N. Wang, X. Zhao and Y. Zhao, Okra-Like Multichannel TiO@NC Fibers Membrane with Spatial and Chemical Restriction on Shuttle-Effect for Lithium–Sulfur Batteries, *Adv. Fiber Mater.*, 2023, **5**, 252–265.
21 B. He, W.-C. Li, Y. Zhang, X.-F. Yu, B. Zhang, F. Li and A.-H. Lu, Paragenesis BN/CNTs hybrid as a monoclinic sulfur host for high rate and ultra-long life lithium–sulfur battery, *J. Mater. Chem. A*, 2018, **6**, 24194–24200.
22 S. Z. Butler, S. M. Hollen, L. Cao, Y. Cui, J. A. Gupta, H. R. Gutiérrez, T. F. Heinz, S. S. Hong, J. Huang, A. F. Ismach, E. Johnston-Halperin, M. Kuno, V. V. Plashnitsa, R. D. Robinson, R. S. Ruoff, S. Salahuddin, J. Shan, L. Shi, M. G. Spencer, M. Terrones, W. Windl and J. E. Goldberger, Progress, Challenges, and Opportunities in Two-Dimensional Materials Beyond Graphene, *ACS Nano*, 2013, **7**, 2898–2926.
23 A. VahidMohammadi, J. Rosen and Y. Gogotsi, The world of two-dimensional carbides and nitrides (MXenes), *Science*, 2021, **372**, eabf1581.
24 H. Lin, X. Wang, L. Yu, Y. Chen and J. Shi, Two-Dimensional Ultrathin MXene Ceramic Nanosheets for Photothermal Conversion, *Nano Lett.*, 2017, **17**, 384–391.
25 J. Ran, G. Gao, F.-T. Li, T.-Y. Ma, A. Du and S.-Z. Qiao, Ti3C2 MXene co-catalyst on metal sulfide photo-absorbers for enhanced visible-light photocatalytic hydrogen production, *Nat. Commun.*, 2017, **8**, 13907.
26 Q. Tao, M. Dahlqvist, J. Lu, S. Kota, R. Meshkian, J. Halim, J. Palisaitis, L. Hultman, M. W. Barsoum, P. O. Å. Persson and J. Rosen, Two-dimensional $Mo_{1.33}C$ MXene with divacancy ordering prepared from parent 3D laminate with in-plane chemical ordering, *Nat. Commun.*, 2017, **8**, 14949.
27 M. Naguib, V. N. Mochalin, M. W. Barsoum and Y. Gogotsi, 25th Anniversary Article: MXenes: A New Family of Two-Dimensional Materials, *Adv. Mater.*, 2014, **26**, 992–1005.
28 M. Naguib, M. Kurtoglu, V. Presser, J. Lu, J. Niu, M. Heon, L. Hultman, Y. Gogotsi and M. W. Barsoum, Two-Dimensional Nanocrystals Produced by Exfoliation of Ti_3AlC_2, *Adv. Mater.*, 2011, **23**, 4248–4253.
29 D. Wang, F. Li, R. Lian, J. Xu, D. Kan, Y. Liu, G. Chen, Y. Gogotsi and Y. Wei, A General Atomic Surface Modification Strategy for Improving Anchoring and Electrocatalysis Behavior of $Ti_3C_2T_2$ MXene in Lithium–Sulfur Batteries, *ACS Nano*, 2019, **13**, 11078–11086.
30 Q. Gu, Y. Cao, J. Chen, Y. Qi, Z. Zhai, M. Lu, N. Huang and B. Zhang, Fluorine-Modulated MXene-Derived Catalysts for Multiphase Sulfur Conversion in Lithium–Sulfur Battery, *Nano-Micro Lett.*, 2024, **16**, 266.
31 X. Liang, A. Garsuch and L. F. Nazar, Sulfur Cathodes Based on Conductive MXene Nanosheets for High-Performance Lithium–Sulfur Batteries, *Angew. Chem., Int. Ed.*, 2015, **54**, 3907–3911.
32 X. Liang, Y. Rangom, C. Y. Kwok, Q. Pang and L. F. Nazar, Interwoven MXene Nanosheet/Carbon-Nanotube Composites as Li–S Cathode Hosts, *Adv. Mater.*, 2017, **29**, 1603040.
33 G. Valurouthu, M. Shekhirev, M. Anayee, R. Wang, K. Matthews, T. Parker, R. W. Lord, D. Zhang, A. Inman, M. Downes, C. W. Ahn, V. Kalra, I.-K. Oh and Y. Gogotsi, Screening Conductive MXenes for Lithium Polysulfide Adsorption, *Adv. Funct. Mater.*, 2024, **34**, 2404430.
34 G. Kresse and J. Furthmüller, Efficiency of *ab initio* total energy calculations for metals and semiconductors using a plane-wave basis set, *Comput. Mater. Sci.*, 1996, **6**, 15–50.
35 J. P. Perdew, K. Burke and M. Ernzerhof, Generalized Gradient Approximation Made Simple, *Phys. Rev. Lett.*, 1996, **77**, 3865–3868.
36 A. Feng, Y. Yu, Y. Wang, F. Jiang, Y. Yu, L. Mi and L. Song, Two-dimensional MXene Ti_3C_2 produced by exfoliation of Ti_3AlC_2, *Mater. Des.*, 2017, **114**, 161–166.
37 M. Li, X. Li, G. Qin, K. Luo, J. Lu, Y. Li, G. Liang, Z. Huang, J. Zhou, L. Hultman, P. Eklund, P. O. Å. Persson, S. Du, Z. Chai, C. Zhi and Q. Huang, Halogenated Ti_3C_2 MXenes with Electrochemically Active Terminals for High-Performance Zinc Ion Batteries, *ACS Nano*, 2021, **15**, 1077–1085.
38 H. Shao, K. Xu, Y.-C. Wu, A. Iadecola, L. Liu, H. Ma, L. Qu, E. Raymundo-Piñero, J. Zhu, Z. Lin, P.-L. Taberna and P. Simon, Unraveling the Charge Storage Mechanism of $Ti_3C_2T_x$ MXene Electrode in Acidic Electrolyte, *ACS Energy Lett.*, 2020, **5**, 2873–2880.
39 J. Li, K. Han, J. Huang, G. Li, S. Peng, N. Li, J. Wang, W. Zhang, Y. Du, Y. Fan, W. Wang and F. Dang, Polarized nucleation and efficient decomposition of Li_2O_2 for Ti_2C MXene cathode catalyst under a mixed surface condition in lithium-oxygen batteries, *Energy Storage Mater.*, 2021, **35**, 669–678.
40 S. Liu, J. Liu, X. Liu, J. Shang, L. Xu, R. Yu and J. Shui, Hydrogen storage in incompletely etched multilayer Ti_2CT_x at room temperature, *Nat. Nanotechnol.*, 2021, **16**, 331–336.

41 M. Cai, H. Yan, Y. Li, W. Li, H. Li, X. Fan and M. Zhu, $Ti_3C_2T_x$/PANI composites with tunable conductivity towards anticorrosion application, *Chem. Eng. J.*, 2021, **410**, 128310.
42 C. Dillard, A. Singh and V. Kalra, Polysulfide Speciation and Electrolyte Interactions in Lithium–Sulfur Batteries with in Situ Infrared Spectroelectrochemistry, *J. Phys. Chem. C*, 2018, **122**, 18195–18203.
43 C. J. Zhang, S. Pinilla, N. McEvoy, C. P. Cullen, B. Anasori, E. Long, S.-H. Park, A. Seral-Ascaso, A. Shmeliov, D. Krishnan, C. Morant, X. Liu, G. S. Duesberg, Y. Gogotsi and V. Nicolosi, Oxidation Stability of Colloidal Two-Dimensional Titanium Carbides (MXenes), *Chem. Mater.*, 2017, **29**, 4848–4856.
44 C. Hou, C. Huang, H. Yu and S. Shi, Surface-Engineered $Ti_3C_2T_x$ with Tunable Work Functions for Highly Efficient Polymer Solar Cells, *Small*, 2022, **18**, 2201046.
45 C. Fan, J. Yang, W. Ni, J. Wu, X. Liu, Z. Li, Y. Zhang, W. Quan, M. Zeng, N. Hu, H. Fang, T. Wang and Z. Yang, Real-Time and Wireless Transmission of a Nitrogen-Doped $Ti_3C_2T_x$ Wearable Gas Sensor for Efficient Detection of Food Spoilage and Ammonia Leakage, *ACS Sens.*, 2024, **9**, 4870–4878.
46 S. Li, P. Tuo, J. Xie, X. Zhang, J. Xu, J. Bao, B. Pan and Y. Xie, Ultrathin MXene nanosheets with rich fluorine termination groups realizing efficient electrocatalytic hydrogen evolution, *Nano Energy*, 2018, **47**, 512–518.
47 Y. Guan, R. Zhao, Y. Cong, K. Chen, J. Wu, H. Zhu, Z. Dong, Q. Zhang, G. Yuan, Y. Li, J. Zhang and X. Li, Flexible Ti_2C MXene film: Synthesis, electrochemical performance and capacitance behavior, *Chem. Eng. J.*, 2022, **433**, 133582.
48 Y. Zhao and J. Zhao, Functional group-dependent anchoring effect of titanium carbide-based MXenes for lithium-sulfur batteries: A computational study, *Appl. Surf. Sci.*, 2017, **412**, 591–598.
49 X. Chen, H. Ji, Z. Rao, L. Yuan, Y. Shen, H. Xu, Z. Li and Y. Huang, Insight into the Fading Mechanism of the Solid-Conversion Sulfur Cathodes and Designing Long Cycle Lithium–Sulfur Batteries, *Adv. Energy Mater.*, 2022, **12**, 2102774.
50 R. Soni, J. B. Robinson, P. R. Shearing, D. J. L. Brett, A. J. E. Rettie and T. S. Miller, Lithium-sulfur battery diagnostics through distribution of relaxation times analysis, *Energy Storage Mater.*, 2022, **51**, 97–107.
51 E. Zhao, K. Nie, X. Yu, Y.-S. Hu, F. Wang, J. Xiao, H. Li and X. Huang, Advanced Characterization Techniques in Promoting Mechanism Understanding for Lithium–Sulfur Batteries, *Adv. Funct. Mater.*, 2018, **28**, 1707543.
52 M. Chen, S. Zhao, S. Jiang, C. Huang, X. Wang, Z. Yang, K. Xiang and Y. Zhang, Suppressing the Polysulfide Shuttle Effect by Heteroatom-Doping for High-Performance Lithium–Sulfur Batteries, *ACS Sustainable Chem. Eng.*, 2018, **6**, 7545–7557.
53 X. Luo, Z. Pu, H. Li, E. Zhao, X. Yang, A. Fu, X. Liu, Y.-G. Guo and H. Li, Preparation of TiO_2 nanoparticles decorated porous carbon via a pseudo co-templating strategy and their application as substrates for high performance cathode of LiS batteries, *J. Energy Storage*, 2024, **102**, 114219.
54 Q. Su, X. Yin, Y. He, Z. Hu, J. Guo, M. Xiang, X. Liu and W. Bai, TiO_2/CNTs dual-decorated functional carbon foam as self-supporting sulfur host for boosting the adsorption and redox kinetics of polysulfides, *J. Alloys Compd.*, 2025, **1010**, 178225.
55 J. Shang, C. Ma, C. Zhang, W. Zhang, B. Shen, F. Wang, S. Guo and S. Yao, Nitrogen-doped carbon encapsulated trimetallic CoNiFe alloy nanoparticles decorated carbon nanotube hybrid composites modified separator for lithium-sulfur batteries, *J. Energy Storage*, 2024, **82**, 110552.
56 X. Men, T. Deng, X. Li, L. Huang and J. Wang, Electrospun carbon nanofibers loaded with sulfur vacancy CoS_2 as separator coating to accelerate sulfur conversion in Lithium-Sulfur batteries, *J. Colloid Interface Sci.*, 2025, **678**, 345–354.
57 Y. Ma, Y. Ren, D. Sun, B. Wang, H. Wu, H. Bian, J. Cao, X. Cao, F. Ding, J. Lu and X. Meng, High entropy alloy nanoparticles dual-decorated with nitrogen-doped carbon and carbon nanotubes as promising electrocatalysts for lithium–sulfur batteries, *J. Mater. Sci. Technol.*, 2024, **188**, 98–104.
58 L.-J. He, J. Liu, T.-T. Lv, A.-C. Wei and T.-Q. Yuan, 1T-rich MoS2 nanosheets anchored on conductive porous carbon as effective polysulfide promoters for lithium–sulfur batteries, *J. Colloid Interface Sci.*, 2024, **671**, 175–183.
59 J. Zhou, S. Sun, X. Zhou, X. Rao, X. Xu, Z. Zhang, Z. Pan, Q.-C. Wang, Z. Wang, Y. Wu, W. D. Wagner, X. Guo, X. Liu, C. Wang, C. Lu and Y. Zhang, Defect engineering enables an advanced separator modification for high-performance lithium-sulfur batteries, *Chem. Eng. J.*, 2024, **487**, 150574.
60 Y. Huang, Y. Wang and Y. Fu, A thermoregulating separator based on black phosphorus/MOFs heterostructure for thermo-stable lithium-sulfur batteries, *Chem. Eng. J.*, 2023, **454**, 140250.
61 Y.-H. Liu, C.-Y. Wang, S.-L. Yang, F.-F. Cao and H. Ye, 3D MXene architectures as sulfur hosts for high-performance lithium-sulfur batteries, *J. Energy Chem.*, 2022, **66**, 429–439.
62 T. Zhang, W. Shao, S. Liu, Z. Song, R. Mao, X. Jin, X. Jian and F. Hu, A flexible design strategy to modify $Ti_3C_2T_x$ MXene surface terminations via nucleophilic substitution for long-life Li-S batteries, *J. Energy Chem.*, 2022, **74**, 349–358.
63 W. Yao, J. Xu, Y. Cao, Y. Meng, Z. Wu, L. Zhan, Y. Wang, Y. Zhang, I. Manke, N. Chen, C. Yang and R. Chen, Dynamic Intercalation–Conversion Site Supported Ultrathin 2D Mesoporous SnO_2/$SnSe_2$ Hybrid as Bifunctional Polysulfide Immobilizer and Lithium Regulator for Lithium–Sulfur Chemistry, *ACS Nano*, 2022, **16**, 10783–10797.
64 T. Li, L. Liang, Z. Chen, J. Zhu and P. Shen, Hollow Ti3C2Tx MXene@$CoSe_2$/N-doped carbon heterostructured composites for multiphase electrocatalysis process in lithium-sulfur batteries, *Chem. Eng. J.*, 2023, **474**, 145970.

65 D. Zhang, S. Wang, R. Hu, J. Gu, Y. Cui, B. Li, W. Chen, C. Liu, J. Shang and S. Yang, Catalytic Conversion of Polysulfides on Single Atom Zinc Implanted MXene toward High-Rate Lithium–Sulfur Batteries, *Adv. Funct. Mater.*, 2020, **30**, 2002471.
66 S. Wei, J. Shang, Y. Zheng, T. Wang, X. Kong, Q. He, Z. Zhang and Y. Zhao, Leveraging doping strategies and interface engineering to enhance catalytic transformation of lithium polysulfides for high-performance lithium-sulfur batteries, *J. Colloid Interface Sci.*, 2024, **675**, 904–914.
67 Y. Zhang, Z. Mu, C. Yang, Z. Xu, S. Zhang, X. Zhang, Y. Li, J. Lai, Z. Sun, Y. Yang, Y. Chao, C. Li, X. Ge, W. Yang and S. Guo, Rational Design of MXene/1T-2H MoS_2-C Nanohybrids for High-Performance Lithium–Sulfur Batteries, *Adv. Funct. Mater.*, 2018, **28**, 1707578.
68 H. Zhang, L. Yang, P. Zhang, C. Lu, D. Sha, B. Yan, W. He, M. Zhou, W. Zhang, L. Pan and Z. Sun, MXene-Derived TiO_2 Quantum Dots Distributed on Porous Carbon Nanosheets for Stable and Long-Life Li–S Batteries: Enhanced Polysulfide Mediation via Defect Engineering, *Adv. Mater.*, 2021, **33**, 2008447.
69 W. Y. Lieu, C. Lin, X. L. Li, S. Jiang, Y. Li, H. Y. Yang and Z. W. Seh, Structural Design of Electrocatalyst-Decorated MXenes on Sulfur Spheres for Lithium–Sulfur Batteries, *Nano Lett.*, 2023, **23**, 5762–5769.
70 R. Liu, S. Zhai, Z. Ye, M. Liu, Y. Xu, C. Li, X. Wang and T. Mei, Constructing carbon nanotube-optimized hollow Ti_3C_2 MXene hierarchical conductive networks for robust lithium–sulfur batteries, *J. Mater. Chem. A*, 2023, **11**, 24330–24337.
71 X. Zhong, D. Wang, J. Sheng, Z. Han, C. Sun, J. Tan, R. Gao, W. Lv, X. Xu, G. Wei, X. Zou and G. Zhou, Freestanding and Sandwich MXene-Based Cathode with Suppressed Lithium Polysulfides Shuttle for Flexible Lithium–Sulfur Batteries, *Nano Lett.*, 2022, **22**, 1207–1216.
72 S. Liu, M. Chen, Y. Luo, Y. He, W. Zhang, Y. Chen, M. Wang, Y. Ye, K. Zhu, Y. Luo, R. Yu, J. Hou, H. Liu, H. Shu and X. Wang, Synergistic electrochemical catalysis by high-entropy metal phosphide in lithium–sulfur batteries, *J. Colloid Interface Sci.*, 2024, **669**, 126–136.
73 Y. Luo, S. Liu, M. Chen, Y. He, W. Zhang, Y. Ye, Y. Chen, M. Wang, Y. Luo, H. Liu, H. Shu, R. Yu and X. Wang, Bimetallic synergistic catalysis strategy with one-dimensional CuCo-NC for enhanced Wide-temperature stability in high-energy lithium-sulfur batteries, *Chem. Eng. J.*, 2025, **505**, 159158.
74 Y. Luo, D. Zhang, Y. He, W. Zhang, S. Liu, K. Zhu, L. Huang, Y. Yang, G. Wang, R. Yu, H. Shu, X. Wang and M. Chen, Intergrated morphology engineering and alloying strategy for FeNi@NC Catalysts: Tackling the polysulfide shuttle in Li-S batteries, *Chem. Eng. J.*, 2023, **474**, 145751.

